











# *Aestivation* motifs explain hypertension and muscle mass loss in mice with psoriatic skin barrier defect

Johannes Wild<sup>1,2</sup>  | Rebecca Jung<sup>1</sup>  | Tanja Knopp<sup>1</sup> | Panagiotis Efentakis<sup>1,3</sup> | Dimitra Benaki<sup>3</sup> | Alexandra Grill<sup>1</sup> | Joanna Wegner<sup>4</sup> | Michael Molitor<sup>1,2</sup>  | Venkata Garlapati<sup>1</sup> | Natalia Rakova<sup>5</sup> | Lajos Markó<sup>6</sup> | Adriana Marton<sup>7</sup>  | Emmanuel Mikros<sup>3</sup> | Thomas Münzel<sup>2</sup>  | Sabine Kossmann<sup>8</sup>  | Manfred Rauh<sup>9</sup> | Daisuke Nakano<sup>10</sup> | Kento Kitada<sup>7,10</sup> | Friedrich Luft<sup>6</sup>  | Ari Waisman<sup>11</sup> | Philip Wenzel<sup>1,2</sup>  | Jens Titze<sup>5,7,12</sup>  | Susanne Karbach<sup>1,2</sup> 

<sup>1</sup>Center for Thrombosis and Hemostasis (CTH), Johannes Gutenberg-University Mainz, Mainz, Germany

<sup>2</sup>Center for Cardiology, Cardiology I, Johannes Gutenberg-University Mainz, Mainz, Germany

<sup>3</sup>Faculty of Pharmacy, University of Athens, Panepistimiopolis of Zographou, Athens, Greece

<sup>4</sup>Department of Dermatology, Johannes Gutenberg-University Mainz, Mainz, Germany

<sup>5</sup>Division of Nephrology and Hypertension, University Clinic Erlangen, Erlangen, Germany

<sup>6</sup>Experimental and Clinical Research Center, Max Delbrück Center for Molecular Medicine, Berlin, Germany

<sup>7</sup>Programme in Cardiovascular and Metabolic Disorders, Duke-NUS Medical School, Singapore, Singapore

<sup>8</sup>Heart Research Institute Sydney, Sydney, Australia

<sup>9</sup>Research Laboratory, Division of Paediatrics, University Clinic Erlangen, Erlangen, Germany

<sup>10</sup>Department of Pharmacology, Faculty of Medicine, Kagawa University, Miki-cho, Kagawa, Japan

<sup>11</sup>Institute for Molecular Medicine, University Medical Center of Mainz, Mainz, Germany

<sup>12</sup>Division of Nephrology, Duke University School of Medicine, Durham, NC, USA

## Correspondence

Johannes Wild, Center for Thrombosis and Hemostasis (CTH), Johannes Gutenberg-University Mainz, Langenbeckstr. 1, 55131 Mainz, Germany.

Email: johannes.wild@unimedizin-mainz.de

Jens Titze, Programme in Cardiovascular and Metabolic Disorders, Duke-NUS Medical School, 8 College Road, Singapore 169856, Singapore.

Email: jens.titze@duke-nus.edu.sg

## Funding information

Bundesministerium für Bildung und Forschung, Grant/Award Number: BMBF01EO1503 and BMBFEDU-V24;

## Abstract

**Aim:** Recent evidence suggests that arterial hypertension could be alternatively explained as a physiological adaptation response to water shortage, termed aestivation, which relies on complex multi-organ metabolic adjustments to prevent dehydration. Here, we tested the hypothesis that chronic water loss across diseased skin leads to similar adaptive water conservation responses as observed in experimental renal failure or high salt diet.

**Methods:** We studied mice with keratinocyte-specific overexpression of IL-17A which develop severe psoriasis-like skin disease. We measured transepidermal water loss and solute and water excretion in the urine. We quantified glomerular filtration rate (GFR) by intravital microscopy, and energy and nitrogen pathways by metabolomics. We measured skin blood flow and transepidermal water loss (TEWL) in conjunction with renal resistive indices and arterial blood pressure.

Jens Titze and Susanne Karbach have equal contribution.

This is an open access article under the terms of the Creative Commons Attribution-NonCommercial-NoDerivs License, which permits use and distribution in any medium, provided the original work is properly cited, the use is non-commercial and no modifications or adaptations are made.

© 2021 The Authors. *Acta Physiologica* published by John Wiley & Sons Ltd on behalf of Scandinavian Physiological Society.

Boehringer Ingelheim Fonds; NIH, Grant/Award Number: RO1HL118579; Renal Research Institute/Duke-NUS; German Federal Ministry for Economics and Technology/DLR Forschung unter Weltraumbedingungen, Grant/Award Number: Mars500-III and 50WB2024; Deutsche Forschungsgemeinschaft, Grant/Award Number: CRC/Transregio156 and DFGKA4035/1-1; Johannes Gutenberg-Universität Mainz

**Results:** Psoriatic animals lost large amounts of water across their defective cutaneous epithelial barrier. Metabolic adaptive water conservation included mobilization of nitrogen and energy from muscle to increase organic osmolyte production, solute-driven maximal anti-diuresis at normal GFR, increased metanephrine and angiotensin 2 levels, and cutaneous vasoconstriction to limit TEWL. Heat exposure led to cutaneous vasodilation and blood pressure normalization without parallel changes in renal resistive index, albeit at the expense of further increased TEWL.

**Conclusion:** Severe cutaneous water loss predisposes psoriatic mice to lethal dehydration. In response to this dehydration stress, the mice activate aestivation-like water conservation motifs to maintain their body hydration status. The circulatory water conservation response explains their arterial hypertension. The nitrogen-dependency of the metabolic water conservation response explains their catabolic muscle wasting.

#### KEYWORDS

aestivation, catabolism, dehydration, double barrier concept, hypertension, transepidermal water loss

## 1 | INTRODUCTION

Current opinion maintains that an important cause of arterial hypertension is an inability of the kidneys to excrete sufficient amounts of salt and water, which functionally couples with an increase in blood vessel tone, and thereby ultimately increases blood pressure. Supporters of the underlying pressure-natriuresis theory for renal long-term blood pressure control contend that adaptive-physiological body responses designed to prevent salt overload and body overhydration provide a unifying pathophysiological explanation for any form of chronic blood pressure increase.<sup>1-3</sup>

Re-testing this widely accepted notion in rats with experimental chronic renal failure, we found that “renal” hypertension was not explained by an inability of the kidneys to excrete sufficient amounts of salt and water.<sup>4</sup> In contrast with the renal salt and water retention theory, we found our rats with experimental kidney mass reduction that the remaining rest of their renal epithelial barrier was able to release the correct amount of salt, but unable to sufficiently conserve water. The resulting “renal” hypertension was caused by an evolutionary-preserved adaptive *aestivation*-like response designed to prevent body dehydration, which utilizes constriction of blood vessels to limit extrarenal water loss.<sup>5</sup> Across the animal kingdom, *aestivators* rely on various hepato-reno-dermal water conservation strategies (metabolic *aestivation* motifs), which allow them to produce and recycle the solutes necessary to keep water in their body.<sup>6-8</sup> In addition, water-conserving *aestivators* centralize their circulation (circulatory *aestivation* motifs) to reduce water loss across the biological barriers, skin and kidney, to a minimum.<sup>5,9,10</sup>

Here, we tested the hypothesis that chronic water loss across the diseased skin might similarly lead to arterial hypertension and muscle mass loss. We show that mice with a psoriasis-like skin barrier disorder lose large amounts of water across their disrupted keratinocyte barrier. In analogy to chronic renal failure, this cutaneous water loss triggers various metabolic and circulatory *aestivation*-like responses that lead to arterial hypertension, and metabolic *aestivation*-like adaptation responses that lead to parallel catabolic muscle wasting.

## 2 | RESULTS

### 2.1 | Transepidermal water loss in experimental psoriasis leads to dehydration

Mammals maintain body fluid balance via concerted action of the four biological barriers kidneys, lung, gut and skin. With an area of approximately 2 m<sup>2</sup> in adults, the skin is the largest organ of the human body.<sup>11,12</sup> The intact skin barrier is relatively impermeable for water, however, transepidermal water loss is significant in injured or diseased skin.<sup>13</sup> Our mouse model of psoriasis mimics the skin phenotype of human psoriasis<sup>14</sup> with its typical features such as hyper- and parakeratosis, thickening of the epidermal and dermal layer, and influx of myeloid cells (Figure 1A,B). Patients with psoriasis show increased transepidermal water loss (TEWL) across their psoriatic plaques.<sup>15</sup> We tested the hypothesis that psoriatic mice suffer from significant water loss across their defective epidermal barrier, which may predispose to dehydration.

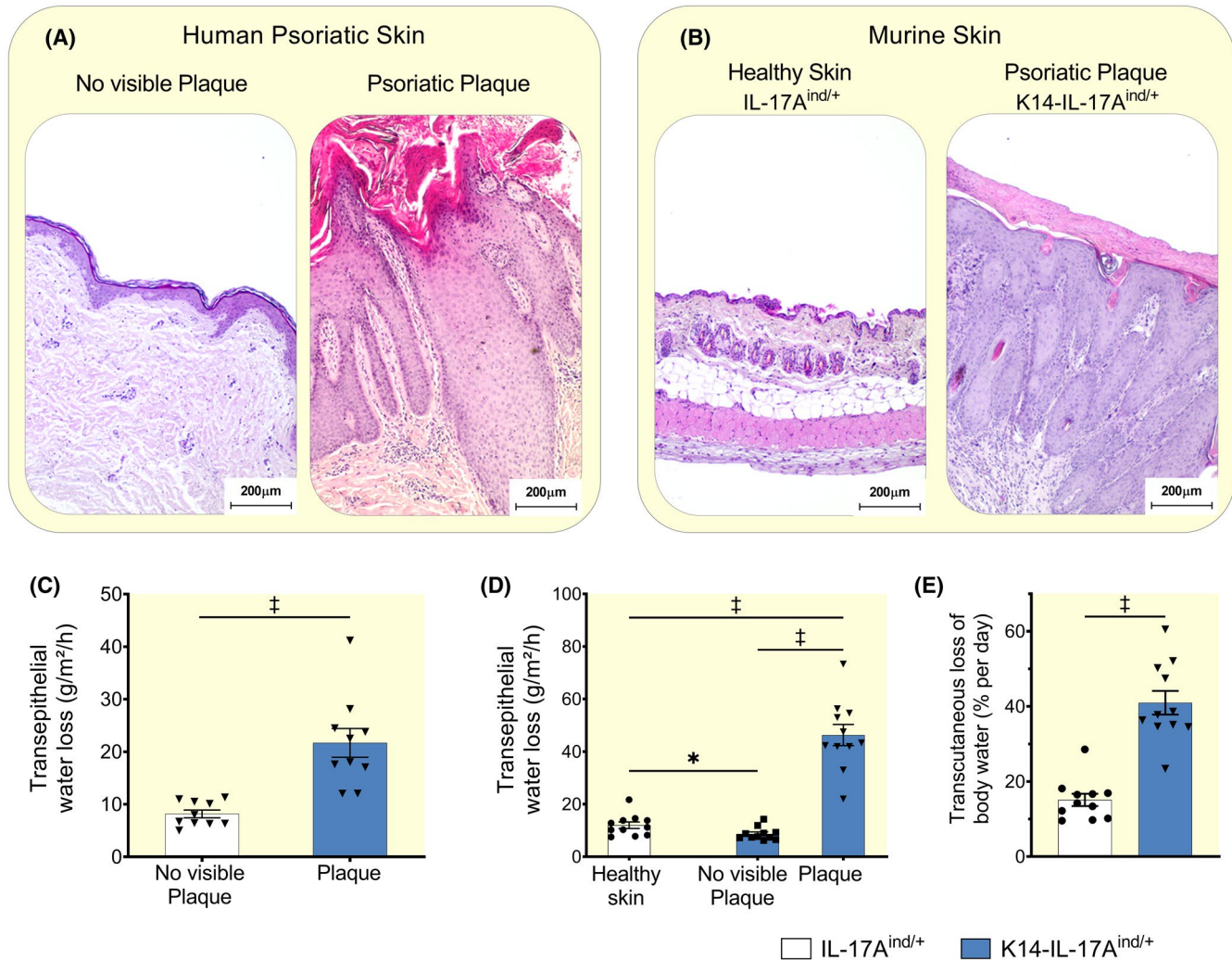


**FIGURE 1** Psoriasis disrupts the skin barrier in human patients and K14-IL-17A<sup>ind/+</sup> mice, which increases transepidermal water loss. A, H&E stained skin sections from non-lesional and lesional human psoriatic skin. Scale bars equal 200  $\mu$ m. B, H&E stained skin sections from healthy skin of IL-17A<sup>ind/+</sup> littermates and skin lesions from K14-IL-17A<sup>ind/+</sup> mice. Scale bars equal 200  $\mu$ m. C, Quantification of transepidermal water loss (TEWL) in skin of psoriatic patients (n = 10). D, Quantification of TEWL in healthy skin of IL-17A<sup>ind/+</sup> littermates (n = 11) and skin of K14-IL-17A<sup>ind/+</sup> mice (n = 11). E, Estimate of daily TEWL, calculated as percentage of total body water in the same mice. For complete data and full calculations see Online Table S1. Data analysis by Student's t-test for independent or dependent samples. Data are shown as mean  $\pm$  SEM. \* $P < .05$ ; † $P < .001$

Similar to patients with psoriasis (Figure 1C), K14-IL-17A<sup>ind/+</sup> animals with keratinocyte-specific overexpression of the cytokine Interleukin-17A (IL-17A) (see method section for details) which develop severe psoriasis-like skin disease, showed increased transepidermal water loss across their psoriatic lesions (Figure 1D). Across the non-affected skin regions, K14-IL17A<sup>ind/+</sup> psoriatic mice showed lower TEWL than their healthy littermate controls (Figure 1D), suggesting a compensatory reduction of TEWL in their intact skin to reduce total skin water loss. However, considering the extent of affected skin surface, mice with severe psoriasis lost in total a calculated amount of  $2.3 \pm 0.5$  mL more water per day through their skin barrier than control mice. Therefore,

K14-IL-17A<sup>ind/+</sup> mice lost daily  $\approx 41\% \pm 10\%$  of their total body water content across their skin, compared to  $15\% \pm 5\%$  in IL-17A<sup>ind/+</sup> control animals with intact skin (Figure 1E and Table S1).

These findings suggest that psoriatic mice have a transepidermal barrier defect, which leads to significant skin water loss and predisposes the animals to dehydration. Physiological adaptation to water shortage, termed *aestivation*, is an evolutionarily conserved survival strategy that relies on complex physiologic-metabolic adjustment to prevent otherwise severe dehydration.<sup>16</sup> We next tested the hypothesis that K14-IL-17A<sup>ind/+</sup> mice utilized circulatory and metabolic aestivation motifs to stabilize their body water content.

## 2.2 | Aestivation motif 1: Reduction in renal solute and water excretion results in adaptive oligo-anuria for stabilization of body water content

Organisms that suffer from dehydration increase their fluid intake and reduce their urine volume to achieve a positive water balance. We hypothesized that besides limiting skin blood flow, K14-IL-17A<sup>ind/+</sup> mice limited renal water loss to compensate for their excessive skin water loss (Figure 1D,E).

Compared to healthy littermates, mice with psoriasis-like skin disease increased their 24-hours water intake and in parallel maximally reduced their 24-hours urine excretion (Figure 2A). Renal barrier function is characterized by

initial water loss because of the glomerular filtration, which is necessary to eliminate surplus body solutes. Most of the filtered solutes are then reabsorbed in the tubular system, mainly as Na<sup>+</sup> (with accompanying anions), K<sup>+</sup> (with accompanying anions) and urea osmolytes. The tubular solute reabsorption process then generates the osmotic driving force necessary for successful tubular water reabsorption and urine concentration.<sup>17</sup>

To test the hypothesis that the massive reduction in urine volume formation in K14-IL-17A<sup>ind/+</sup> mice might be explained by reduced glomerular filtration rate, we imaged glomerular filtration and quantified tubular flow (Video S1 and Video S2). Compared to healthy littermates, psoriatic mice showed similar flow rates in the proximal tubules

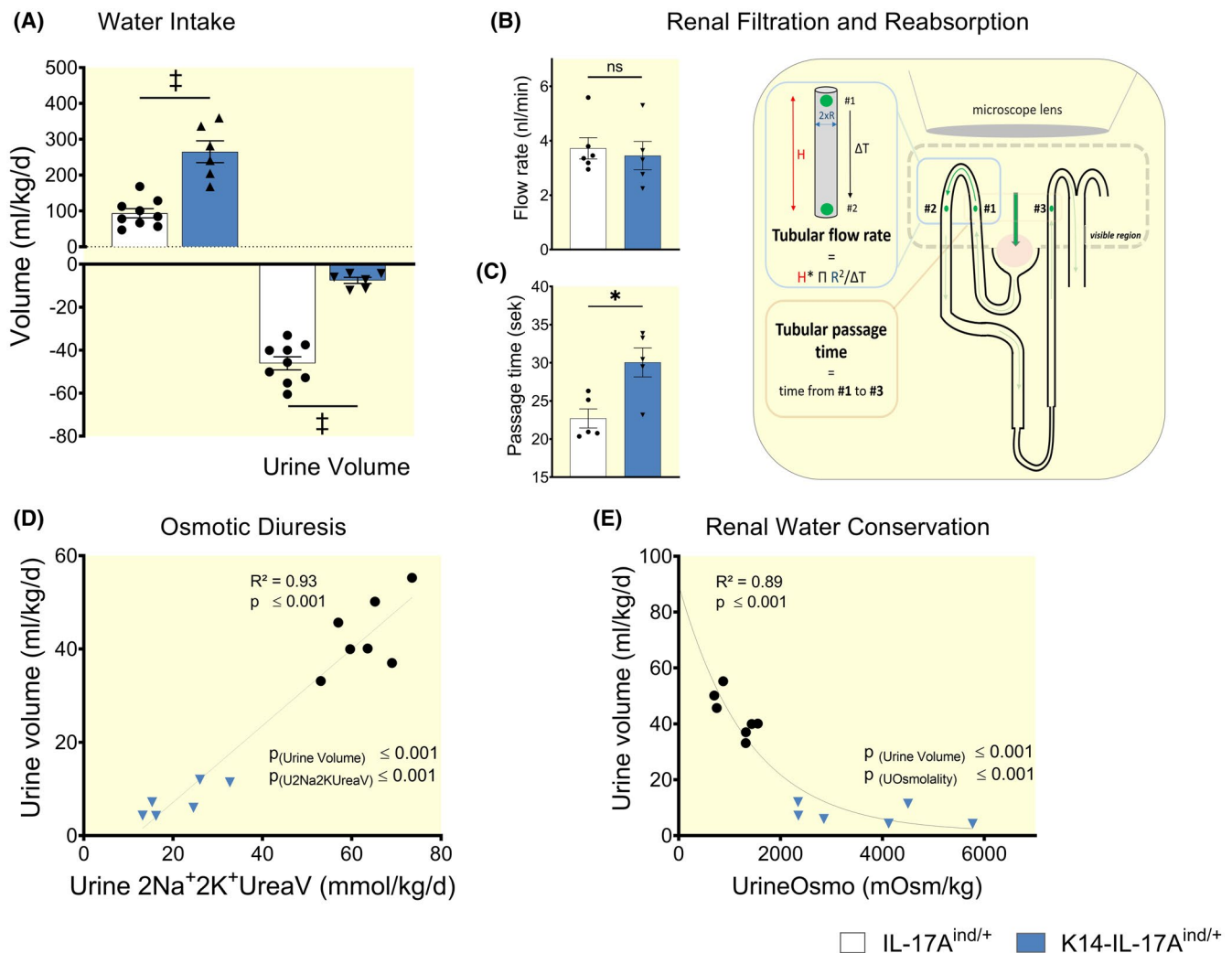


**FIGURE 2** K14-IL-17A<sup>ind/+</sup> mice successfully compensate their dermal water loss by reducing renal solute excretion and strengthening their urine concentration mechanism. A, Fluid intake and urine excretion in IL-17A<sup>ind/+</sup> (n = 9) and K14-IL-17A<sup>ind/+</sup> mice (n = 6). B, Glomerular filtration rate, measured as proximal tubular flow rate by intravital microscopy of kidney tubules in IL-17A<sup>ind/+</sup> (n = 5) and K14-IL-17A<sup>ind/+</sup> mice (n = 5). C, Ultrafiltrate passage time from proximal to distal tubule in the same mice. D, Relationship between  $2Na^+2K^+$  (calculated twofold to account for the excretion of unmeasured accompanying anions), urea solute excretion and urine volume formation in IL-17A<sup>ind/+</sup> (n = 7) and K14-IL-17A<sup>ind/+</sup> mice (n = 6). E, Relationship between urine osmolality and urine volume formation in the same animals as in Panel D. Data analysis by simple linear regression or Student's *t* test for independent samples. Data are shown as mean  $\pm$  SEM. \**P* < .05; †*P* < .001



(Figure 2B), indicating normal glomerular filtration rate. In line with these functional intra-vital findings, histology showed no evidence of kidney damage (Figure S1A,B), and the mice had no proteinuria (Figure S1C). We measured longer passage times of the primary filtrate from proximal to distal tubules in K14-IL-17A<sup>ind/+</sup> mice (Figure 2C), indicating reduced tubular flow rates despite similar glomerular filtration rate. We conclude that K14-IL-17A<sup>ind/+</sup> mice reduced their urine volume to almost anuric levels by massive tubular water reabsorption.

Compared to their littermate controls, psoriatic animals reduced the amount of daily excreted Na<sup>+</sup>, K<sup>+</sup> and urea solutes (cation osmolyte excretion calculated twofold to account for accompanying anions), by 66.2% (Figure 2D), and thereby prevented osmotic diuresis. Furthermore, psoriatic mice showed a two- to sixfold increase in urine osmolality, indicating further urine volume reduction by maximum urine concentration (Figure 2E) and a reduction in 24-hours Na<sup>+</sup>, K<sup>+</sup>, and urea solute excretion (Figure S2A). The relative contribution of the excreted Na<sup>+</sup>, K<sup>+</sup>, and urea solutes to total urine solute excretion revealed that psoriatic mice predominantly retained urea solutes (Figure S2B).

These findings indicate that K14-IL-17A<sup>ind/+</sup> mice had healthy kidneys which reduced solute excretion and enforced urine concentration for renal water conservation. We conclude that the animals utilized water conservation in the renal barrier to its physiological limits to compensate for the water loss that occurred across their defective skin barrier. Because of the predominant reduction of urinary urea in this water conservation process, we next studied urea metabolism in the kidney and the skin (Figure 3).

### 2.3 | Aestivation motif 2: Increased urea transport for water conservation in the epithelial kidney and skin barrier

Water conservation in the renal concentration segment relies on the transport of urea osmolytes by the urea transporter A1 (UTA-1) in the renal medulla.<sup>18</sup> K14-IL-17A<sup>ind/+</sup> mice showed increased UT-A1 mRNA (Figure S3A) and protein levels in their kidneys (Figure 3A), resulting in increased urea osmolyte content in the renal urine concentration segment (Figure 3B). K14-IL-17A<sup>ind/+</sup> mice coupled increased UT-A1-driven urea transport with increased aquaporin-2 (*Aqp2*) mRNA expression (Figure 3C), indicating that the mice facilitated urea-driven water reabsorption in the renal medulla by improving channel-mediated water permeability in the collecting duct. Increased renal water conservation by urine concentration in K14-IL-17A<sup>ind/+</sup> mice appeared to be UT-A1- and AQP2-specific, as mRNA-expression of UT-A2 and the other aquaporins were not different between control and K14-IL-17A<sup>ind/+</sup> mice (Figure S3A,B).

In response to dehydration, tonicity enhancer-binding protein (TonEBP) improves the kidney's ability to concentrate the urine by increasing UT-A1<sup>19</sup> and AQP2 levels<sup>20</sup> in the tubular cells of the collecting duct. We detected elevated TonEBP protein level in kidney of K14-IL-17A<sup>ind/+</sup> mice (Figure 3A), indicating that dermal water loss had strengthened their renal concentration mechanism in the tubular epithelium of the collecting duct by known responses of mammals experiencing water shortage of any sort.<sup>21-23</sup>

Similar to the findings in their water-conserving intact renal epithelial barrier, K14-IL-17A<sup>ind/+</sup> mice showed increased skin UT-A1 expression (Figure 3D), resulting in high skin urea levels (Figure 3E). Furthermore, we found increased mRNA levels of Aquaporin 3 (*Aqp3*; Figure 3F), which is the most abundant aquaglyceroporin in the skin.<sup>24</sup> Western blot analysis and immunofluorescence stainings of psoriatic skin revealed increased TonEBP expression in skin of K14-IL-17A<sup>ind/+</sup> mice (Figure 3D), which was not limited to invading CD45-positive immune cells,<sup>25,26</sup> but also present in skin keratinocytes (Figure 3G).

Besides urea, K14-IL-17A<sup>ind/+</sup> mice accumulated significant amounts of Na<sup>+</sup> at the total body level (Figure S4A). The large Na<sup>+</sup> accumulation was paralleled by only small increases in their plasma Na<sup>+</sup> concentration (Figure S4B) which confirmed previous findings.<sup>27</sup> Despite the marked enhancement of UTA1 protein expression in the kidney and the skin, we could neither detect increased plasma urea levels (Figure S4B) nor elevated plasma osmolality (Figure S4C) in K14-IL-17A<sup>ind/+</sup> mice.

Compared to their healthy littermates, K14-IL-17A<sup>ind/+</sup> mice showed increased water content in their skin and their skinned rest carcass, resulting in increased total body water content (Figure 3H and Table S2). We interpret these findings to show that in an effort to limit transepidermal fluid evaporation across their disrupted epithelial barrier, K14-IL-17A<sup>ind/+</sup> mice utilized water conservation regimes in their kidneys and their skin that were driven by comparable expression and adaptation of urea transporters and aquaporins. Forslund et al have reported earlier that the epidermal epithelium generates electrolyte gradients which may support transepidermal water conservation.<sup>28-34</sup> In the absence of microanatomical resolution measurements of urea concentrations, we can only speculate that K14-IL-17A<sup>ind/+</sup> mice utilized increased cutaneous urea transport for water conservation across skin regions in which their epidermal barrier was not disrupted. Our chemical analysis (Table S2), however, indicates that despite substantial transepidermal water loss across skin areas with a disrupted epidermal barrier, K14-IL-17A<sup>ind/+</sup> mice employed multiple adaptive renal and extrarenal water conservation responses which were such powerful that their activation ultimately resulted in increased body water content per dry mass and per total weight.

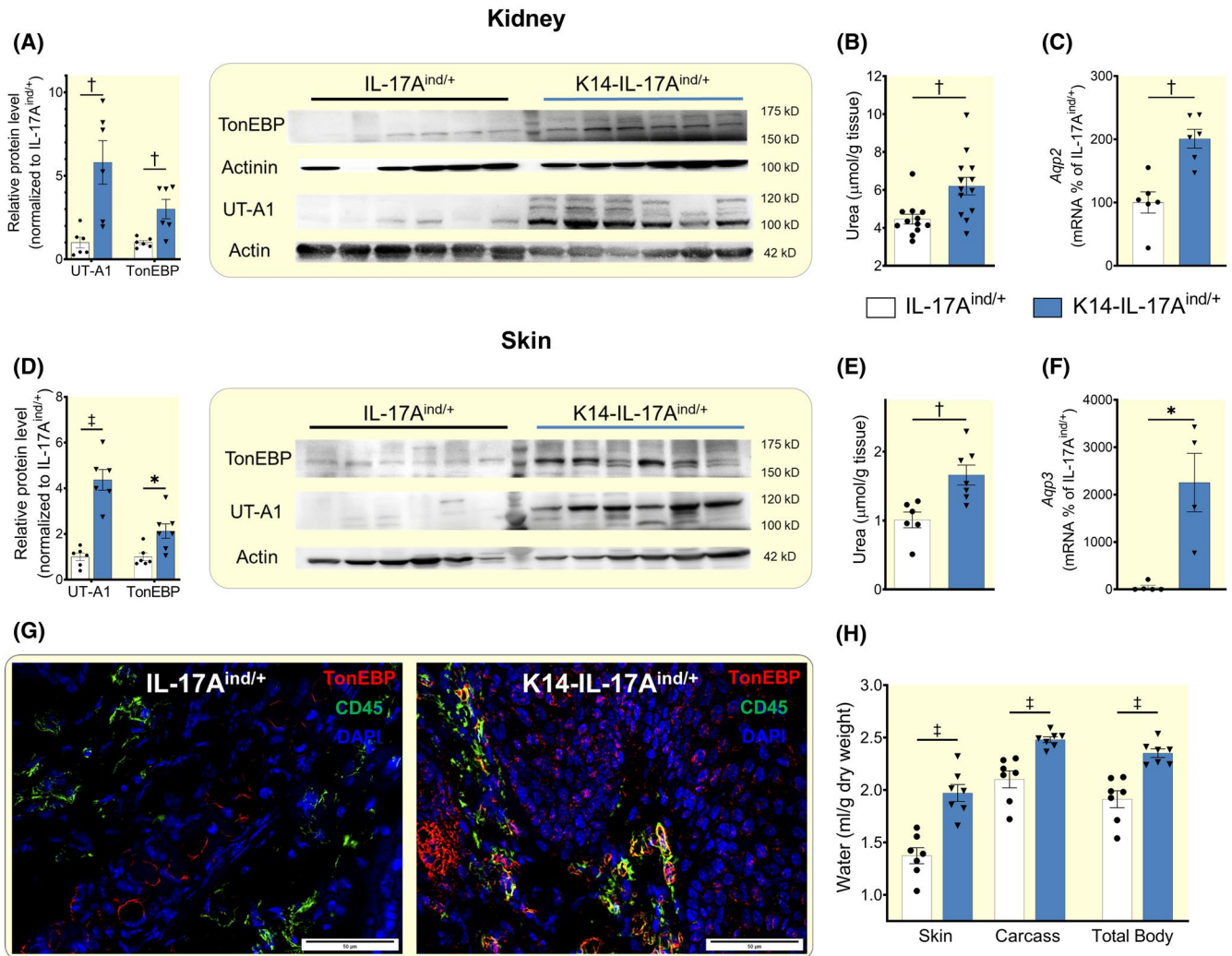


**FIGURE 3** K14-IL-17A<sup>ind/+</sup> mice utilize urea- and water transport mechanisms in kidney and skin to successfully prevent body dehydration. A, Urea transporter A1 (UT-A1) and tonicity enhancer binding protein (TonEBP) protein expression in the kidney of IL-17A<sup>ind/+</sup> (n = 6) and K14-IL-17A<sup>ind/+</sup> mice (n = 6). B, Urea content in the kidney of IL-17A<sup>ind/+</sup> (n = 12) and K14-IL-17A<sup>ind/+</sup> mice (n = 12). C, Expression of Aquaporin 2 mRNA in kidneys of IL-17A<sup>ind/+</sup> (n = 5) and K14-IL-17A<sup>ind/+</sup> mice (n = 5). D, UT-A1 and TonEBP protein expression in the skin of IL-17A<sup>ind/+</sup> (n = 6) and K14-IL-17A<sup>ind/+</sup> mice (n = 6). E, Urea content in skin of IL-17A<sup>ind/+</sup> (n = 6) and K14-IL-17A<sup>ind/+</sup> mice (n = 6). F, Expression of Aquaporin 3 mRNA in skin of IL-17A<sup>ind/+</sup> (n = 5) and K14-IL-17A<sup>ind/+</sup> mice (n = 5). G, Immunofluorescence stained skin sections from healthy IL-17A<sup>ind/+</sup> control and psoriatic K14-IL-17A<sup>ind/+</sup> mice (red: TonEBP; green: CD-45; blue: DAPI). Scale bars equal 50 μm. (H) Tissue water content in skin, carcass and whole body of IL-17A<sup>ind/+</sup> (n = 7) and K14-IL-17A<sup>ind/+</sup> (n = 7) animals. For additional data about total body and tissue water see Online Table S2. Data analysis by Student's *t* test for independent samples. Data are shown as mean ± SEM. \* *P* < .05; † *P* < .01; ‡ *P* < .001

## 2.4 | Aestivation motif 3: Energy and nitrogen transfer from muscle to liver for urea osmolyte generation

We have reported earlier that successful water conservation, besides efficient transporter-mediated osmolyte accumulation in the epithelial kidney barrier, additionally requires increased urea osmolyte synthesis in the liver.<sup>35</sup> Such hepatorenal regulation of body water homeostasis links body fluid homeostasis with systemic energy metabolism. Increased production of urea and other organic osmolytes is energy

intense and involves utilization of endogenous amino acids stored in muscle protein, which provide with the carbon and nitrogen components necessary for successful organic osmolyte synthesis in the liver. We tested the hypothesis that stabilization of body water content we had observed in K14-IL-17A<sup>ind/+</sup> mice involved hepatic urea osmolyte synthesis.

Compared to their healthy controls, K14-IL-17A<sup>ind/+</sup> mice increased their food intake (2.7 ± 0.7 KJ/kg/d vs 4.1 ± 0.67 KJ/kg/d; *P* < .01) at lower body weight (23.5 ± 4.1g v 14.7 ± 1.9g; *P* < .01). We conclude that K14-IL-17A<sup>ind/+</sup> mice showed a catabolic metabolic state. We therefore next

studied the metabolic checkpoints of protein mobilization from skeletal muscle in K14-IL-17A<sup>ind/+</sup> mice. K14-IL-17A<sup>ind/+</sup> mice showed signs of muscle catabolism with decreased muscle mass (Figure 4A), increased total and nuclear glucocorticoid receptor protein expression (Figure 4B and Figure S5), reduced liver glucose and mannose levels indicating gluconeogenesis with a reduction in liver glycogen stores (Figure 4C), and increased 3-OH-butyrate levels (Figure 4C), suggesting a switch from energy-intense gluconeogenesis to energy-efficient hepatic ketogenesis. However, despite this glucocorticoid-driven catabolic state, K14-IL-17A<sup>ind/+</sup> mice showed a 50% increase in liver mass (Figure 4A) with

no signs of hepatic energy deficit, as their phosphorylated protein levels of the cellular energy sensor, AMP-activated kinase (AMPK), were not different from healthy controls (Figure 4D).

We next tested the hypothesis that liver hypertrophy might result in increased amino acid-driven ureagenesis for water conservation in K14-IL-17A<sup>ind/+</sup> mice. The metabolic signature of catabolic exploitation of muscle protein is characterized by the mobilization of the branched-chain amino acids (BCAAs) valine, leucine and isoleucine from muscle protein.<sup>25</sup> Similarly, the muscle dipeptides anserine and carnosine, which serve as a muscle energy store that is

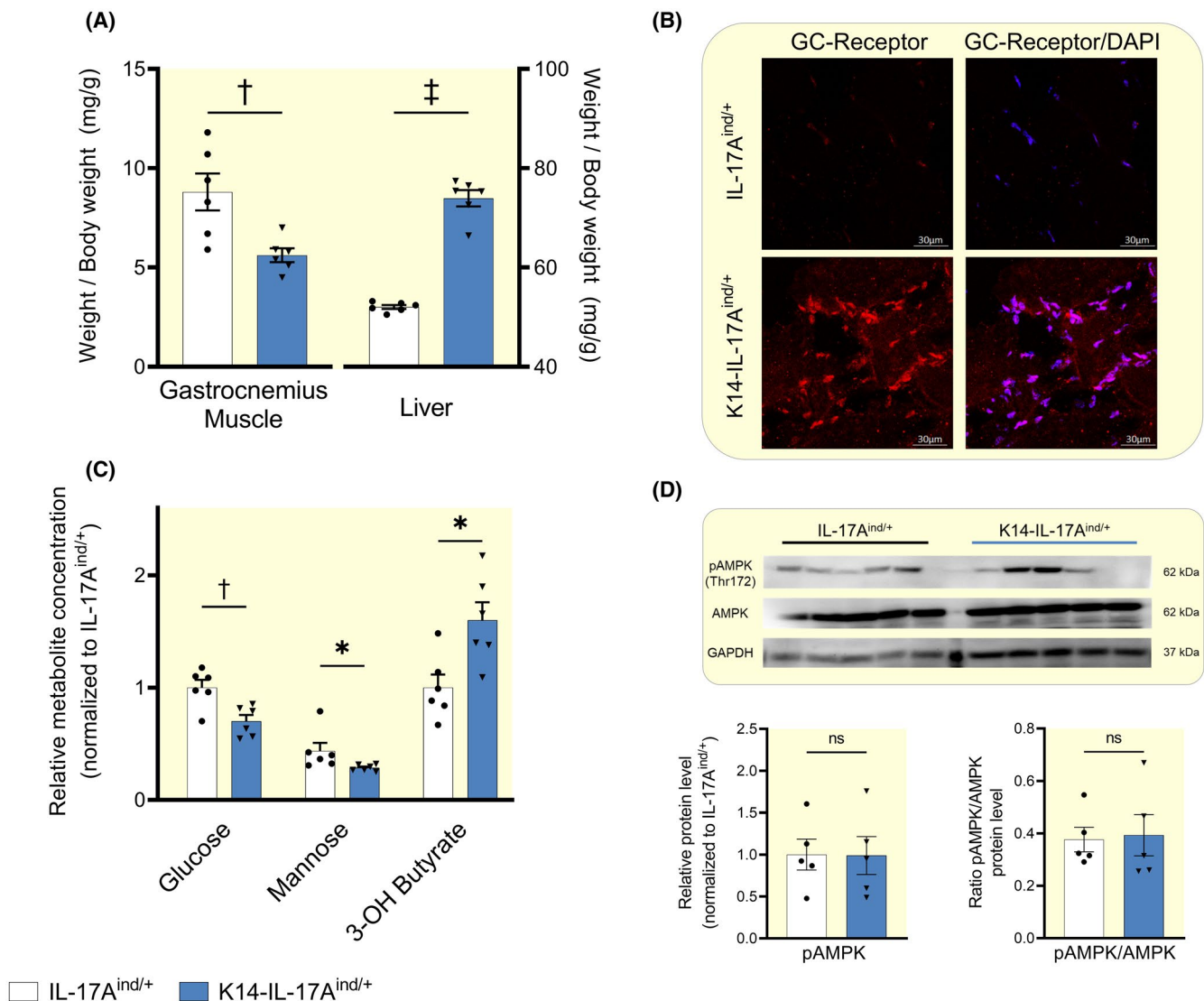


**FIGURE 4** Nitrogen transfer from catabolic skeletal muscle results in liver hypertrophy in K14-IL-17A<sup>ind/+</sup> mice. A, Relative organ weight of gastrocnemius muscle and liver normalized to body weight of IL-17A<sup>ind/+</sup> (n = 6) and K14-IL-17A<sup>ind/+</sup> (n = 6) mice. B, Representative immunofluorescence staining of glucocorticoid receptor (red; left panel); and parallel glucocorticoid receptor and DAPI (blue) staining in an IL-17A<sup>ind/+</sup> and a K14-IL-17A<sup>ind/+</sup> mouse. Scale bars equal 30 μm. C, Analysis of metabolites of hepatic energy transfer in IL-17A<sup>ind/+</sup> (n = 6) and K14-IL-17A<sup>ind/+</sup> (n = 6) mice. D, Hepatic protein expression of unphosphorylated (AMPK) and phosphorylated AMP-activated kinase (pAMPK) in liver of IL-17A<sup>ind/+</sup> (n = 5) and K14-IL-17A<sup>ind/+</sup> (n = 5) mice. Data are analysed by Student's *t* test for independent samples. Data are shown as mean ± SEM. \**P* < .05; †*P* < .01; ‡*P* < .001

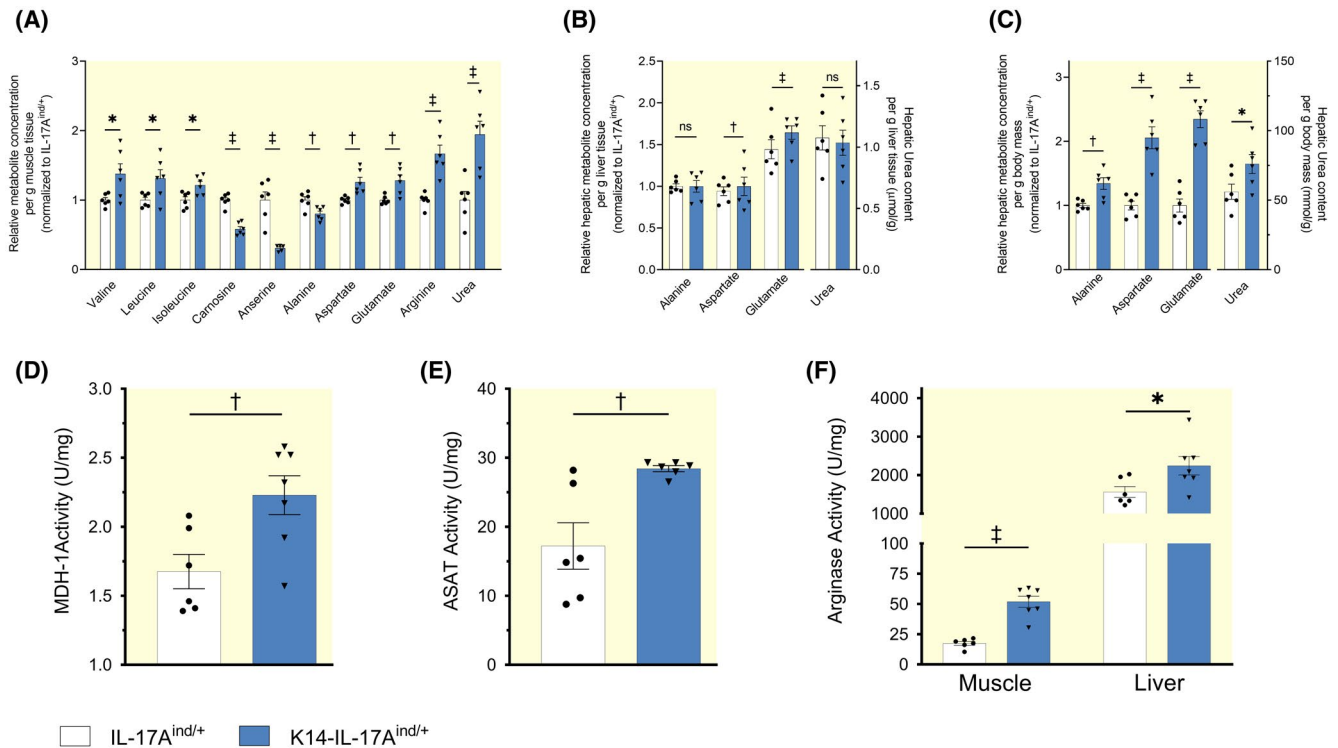


**FIGURE 5** Chronic skin water loss triggers liver and muscle urea osmolyte generation for water conservation. A, Analysis of metabolites participating in amino acid-driven mobilization of energy and nitrogen from skeletal muscle in IL-17A<sup>ind/+</sup> (n = 6) and K14-IL-17A<sup>ind/+</sup> mice (n = 6). B, Analysis of metabolites of hepatic nitrogen transfer per g liver tissue in the same mice. Alanine, Aspartate and Glutamate levels were normalized to the average level of IL-17A<sup>ind/+</sup> mice, Urea content is presented as non-normalized amount per g liver tissue. C, Analysis of hepatic metabolites per g body mass in the same mice. Alanine, Aspartate and Glutamate levels were normalized to the average level of IL-17A<sup>ind/+</sup> mice, Urea content is presented as non-normalized amount per g body mass. D, Enzyme activity of cytoplasmic malate dehydrogenase 1 (MDH-1); E, aspartate aminotransferase (ASAT) and in gastrocnemius muscle IL-17A<sup>ind/+</sup> (n = 6) and K14-IL-17A<sup>ind/+</sup> (n = 6) mice. F, Enzyme activity of arginase in gastrocnemius muscle and liver in the same mice as in Panel D/E. Data are analysed by Student's *t* test for independent samples. Data are shown as mean  $\pm$  SEM. \**P* < .05; †*P* < .01; ‡*P* < .001

not integrated into muscle fibre, are exploited for energy and nitrogen transfer into the liver (Figure S6). We found increased BCAA content and reduced anserine and carnosine levels in K14-IL-17A<sup>ind/+</sup> mice (Figure 5A). K14-IL-17A<sup>ind/+</sup> mice furthermore showed increased glutamate, aspartate, arginine and urea levels, suggesting increased transamination and extrahepatic urea solute production in skeletal muscle (Figure 5A). Per gram tissue mass, we found reduced alanine levels in muscle (Figure 5A), and elevated aspartate and glutamate levels in the livers of K14-IL-17A<sup>ind/+</sup> mice (Figure 5B). Due to the observed liver hypertrophy, liver amino acid and urea content per g body mass were therefore 1.4- to 2.5-fold higher in K14-IL-17A<sup>ind/+</sup> mice than in controls (Figure 5C).

We finally tested for differences in the enzymatic transamination machinery between K14-IL-17A<sup>ind/+</sup> and control mice. Transfer of amino acid energy from muscle to liver is organized by the glucose-alanine-nitrogen shuttle,<sup>36,37</sup> which depends on a successful transamination cascade to ultimately form alanine (C3-amino acid) from pyruvate (corresponding C3-carbon acid). Besides transamination,

this transfer process relies on the generation of the carbonic acid oxaloacetate (OxA) from malate (Mal), catalysed by the cytoplasmic form of the enzyme malate dehydrogenase (MDH1), and followed by transamination of oxaloacetate to aspartate (Figures S6 and S7). This transamination step is catalysed by the cytoplasmic enzyme aspartate aminotransferase (ASAT). In muscle, K14-IL-17A<sup>ind/+</sup> mice increased their cytoplasmic oxaloacetate (C4 carbonic acid) generation by increasing MDH1 enzyme activity (Figure 5D). An additional increase in ASAT enzyme activity (Figure 5E) promoted the generation of its corresponding C4-amino acid aspartate (Figure 5A). We conclude that activation of the transamination machinery in skeletal muscle supported the generation of alanine from pyruvate (C3 amino acid with its corresponding carbonic acid), of aspartate from oxaloacetate, and of glutamate from  $\alpha$ -ketoglutarate (c-5 amino acid with its corresponding carbonic acid). This catabolic process was accompanied by increased arginase activity (Figure 5F), indicating enhanced extrahepatic urea osmolyte production from elevated arginine levels. Hepatic arginase activity was 20-fold



higher than in skeletal muscle and elevated in K14-IL-17A<sup>ind/+</sup> mice (Figure 5F). We interpret these findings to show the exploitation of muscle energy and nitrogen reservoirs for subsequent transfer to the liver via the glucose-alanine-nitrogen shuttle.

## 2.5 | Aestivation motif 4: Circulatory adjustment in skin blood flow limits transepidermal water loss, but results in arterial hypertension

Systemic vasoconstriction is a fundamental physiological component for the maintenance of body fluid homeostasis. Vasoconstriction in the renal vascular beds reduces the size of the urine volume,<sup>38</sup> whereas vasoconstriction of the cutaneous counter current vessels reduces dermal blood flow and thereby limits transepidermal water loss.<sup>39-41</sup> We tested the hypothesis that in an effort to prevent further water loss

across the skin, K14-IL-17A<sup>ind/+</sup> mice reduced their dermal blood flow by vasoconstriction, and thereby reduced TEWL across the unaffected skin regions.

Compared to their healthy controls, K14-IL-17A<sup>ind/+</sup> mice at normal body temperature showed lower transepidermal water loss in skin regions without visible plaque formation (Figures 1D and 6A). In line with our hypothesis, the TEWL reduction in K14-IL-17A<sup>ind/+</sup> mice was paralleled by reduced pedal skin blood perfusion (Figure 6B), indicating increased dermal vasoconstriction for body fluid conservation. Similarly, K14-IL-17A<sup>ind/+</sup> mice showed increased renal resistance indexes, indicating parallel vasoconstriction of the renal vascular bed (Figure 6A). Increased vasoconstriction in K14-IL-17A<sup>ind/+</sup> mice was paralleled by increased angiotensin 2 and metanephrine serum levels, suggesting generalized systemic vasoconstriction via hormonal and neural vasoconstriction signals (Figure 6C). Similar to all organisms with increased vascular tone, K14-IL-17A<sup>ind/+</sup> mice indeed showed increased arterial blood pressure (Figure 6A), despite

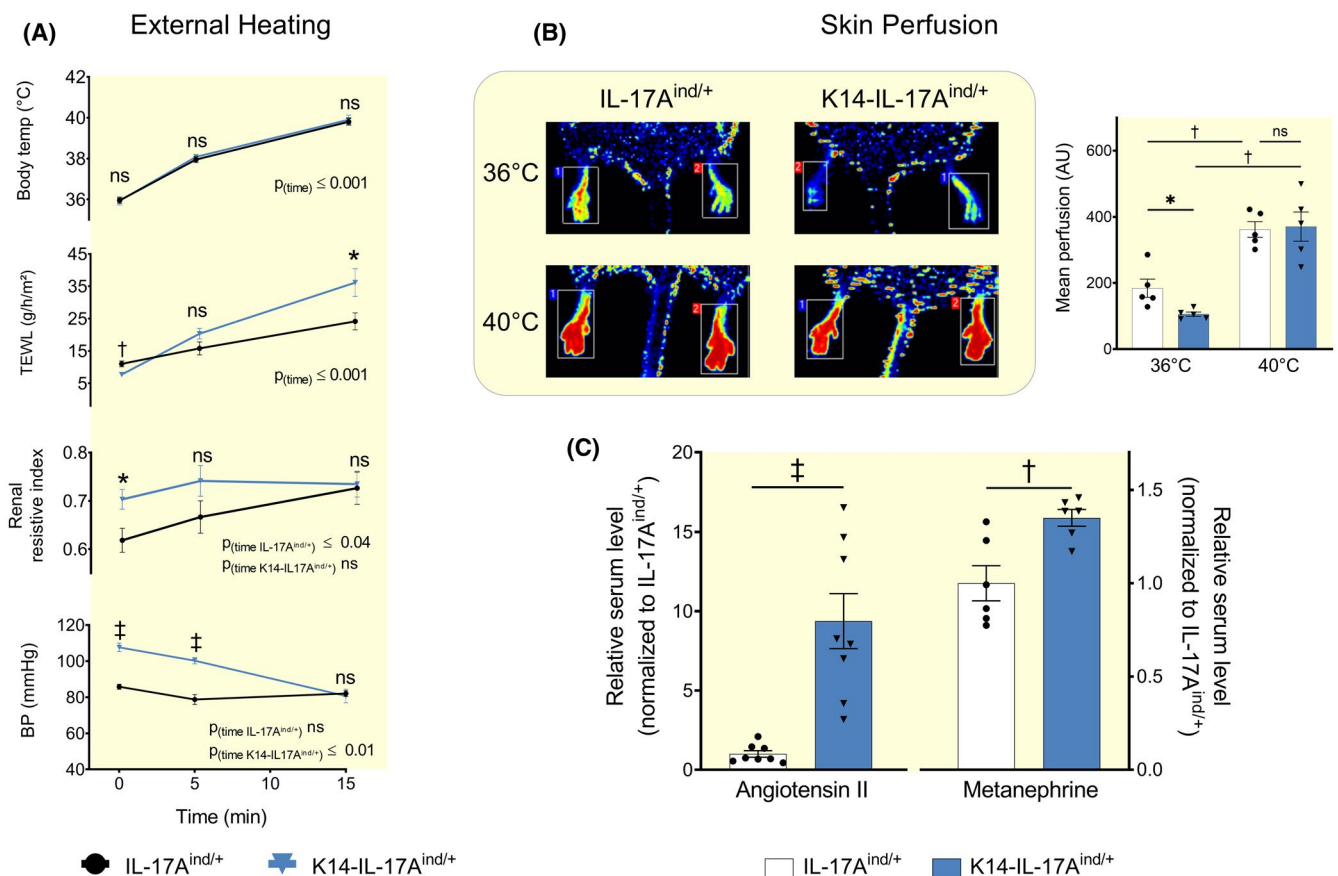


**FIGURE 6** Dermal vasoconstriction for water conservation elevates systolic blood pressure in K14-IL-17A<sup>ind/+</sup> mice. A, Effect of external heating on blood pressure in IL-17A<sup>ind/+</sup> (n = 6) and K14-IL-17A<sup>ind/+</sup> mice (n = 6). We show parallel changes in body core temperature, TEWL of unaffected skin regions, renal resistive index and blood pressure. B, Representative Laser Doppler measurements of mean skin perfusion index of a control animal (left) and of unaffected skin from a psoriatic animal (right) at 36°C (upper) and 40°C (lower). Quantification of temperature-dependent changes in skin perfusion in IL-17A<sup>ind/+</sup> (n = 5) and K14-IL-17A<sup>ind/+</sup> mice (n = 5). C, Serum angiotensin II (Ang II) and metanephrine levels in IL-17A<sup>ind/+</sup> (n = 8) and K14-IL-17A<sup>ind/+</sup> mice (n = 8). Serum levels were normalized to the average level of all healthy animals. Data analysis by Student's t-test for independent or dependent samples. Data are shown as mean ± SEM. \*P < .05; †P < .01; ‡P < .001

the continuous water loss across the transepidermal barrier (Figure 1D,E).

Besides water conservation, the skin barrier also plays a key role in body temperature regulation.<sup>40</sup> Homoeothermic mice vasodilate skin vessels to increase TEWL and utilize the resulting evaporative cooling to stabilize their body temperature in the heat, albeit at the expense of body water loss. We hypothesized that dermal vasoconstriction for cutaneous body fluid conservation significantly elevates blood pressure in K14-IL-17A<sup>ind/+</sup> mice. To test this hypothesis, we anaesthetized our mice and increased their body temperature by 4°C within 15 minutes by exposure to red light. With elevating body temperature, both K14-IL-17A<sup>ind/+</sup> and control mice increased their skin perfusion, and the pre-existing difference in their skin blood mass disappeared (Figure 6B). The resulting steeper increase in skin perfusion in K14-IL-17A<sup>ind/+</sup> mice normalized their systemic blood pressure level, albeit at the expense of increased skin water loss (Figure 6A). In control mice, temperature exposure induced renal vasoconstriction (Figure 6A). Within 15 minutes, control mice had increased their renal resistive indexes to the level of K14-IL-17A<sup>ind/+</sup> mice. In contrast with control mice, temperature exposure did not further elevate the pre-existing high renal resistive indexes in K14-IL-17A<sup>ind/+</sup> mice. We conclude that temperature exposure vasodilated skin vessels in K14-IL-17A<sup>ind/+</sup> mice, while the level of vasoconstriction in the renal vascular bed did not change. The temperature-induced changes in systemic blood pressure in K14-IL-17A<sup>ind/+</sup> mice therefore were not attributable to renal circulatory adjustment.

We interpret these findings to show that K14-IL-17A<sup>ind/+</sup> mice constricted cutaneous blood vessels in an effort to limit elevated water loss across their leaky epidermal barrier. This dermal water conservation response occurred at the expense of arterial hypertension.

### 3 | DISCUSSION

We have found that “renal” hypertension that occurs in experimental renal failure cannot be explained easily by a body response that is secondary to renal water loss.<sup>4</sup> Because this concept is antipodal to current understanding on the relationship between body fluid and blood pressure homeostasis, we additionally tested the hypothesis that water loss across the disrupted skin barrier in mice with psoriasis-like skin disease would similarly trigger evolutionary-preserved *aestivation*-like patterns for water conservation, and explain hypertension.

In line with this hypothesis, we find that the hypertension in K14-IL-17A<sup>ind/+</sup> mice is explained by vasoconstriction of dermal blood vessels in an effort to limit transepidermal water loss across the disrupted epithelial barrier. We

have previously tried to explain the arterial hypertension in K14-IL-17A<sup>ind/+</sup> mice by immune cell-driven induction of vascular dysfunction.<sup>27</sup> However, our recent finding that T-cell-specific overexpression of IL-17A resulted in similar vascular dysfunction and reactive oxygen generation without exerting any blood pressure change casts doubt on the concept that immune cell- or interleukin-driven effects on the vasculature are sufficient to causally explain arterial hypertension.<sup>42</sup> Our data instead suggest that vasoconstriction because of reduced vascular endothelial NO synthesis and increased reactive oxygen species may be a logical consequence of a systemic reprioritization of energy and nitrogen metabolism for successful water conservation by adaptive *aestivation* motifs. Our temperature exposure experiments additionally show that such metabolically driven vasoconstriction for water conservation does not “clamp” blood pressure in psoriatic mice at high levels. In contrast, the mice can rapidly abandon their dermal vasoconstriction once thermic energy needs to be released via the skin.

This acute change in skin vascular function is most likely explained by a dominating effect of sympathetic skin nerves, which apparently can override any underlying metabolic endothelial dysfunction by rapidly reducing their discharge.<sup>43</sup> This hierarchy allows the organism to acutely dilate skin blood vessels once facilitated heat release across the skin is mandatory. We conclude that the idea of a dermato-renal maintenance of body fluid homeostasis, which is a well-established *aestivation* motif, may provide a simple alternative view towards a better understanding of the underlying cause of arterial hypertension (Figure S8): once the dermal vasoconstriction necessary for improved transepidermal water conservation is abolished, blood pressure levels normalize, albeit at the expense of increased skin water loss. While the effect of dermal skin vasodilation on increasing transepidermal water loss and reducing core body temperature is a well-established physiological concept, we cannot exclude that parallel decreases in cardiac output may have additionally contributed to the blood pressure-lowering effect that we observed in our mouse model of psoriasis hypertension.

We additionally show that chronic skin barrier failure induces a hepato-reno-dermal *aestivation* motif, which consists of increased urea osmolyte production in liver and muscle. The increase in organic osmolyte production is coupled with increased transporter-driven urea osmolyte accumulation in the skin and kidney barriers to limit transepithelial water loss. The energy and nitrogen-intense nature of this compensatory increase in organic solute production explains why K14-IL-17A<sup>ind/+</sup> mice live in a starvation state with catabolic muscle wasting despite increased food intake. We conclude that chronic water loss across a defective skin or kidney barrier not only triggers compensatory circulatory *aestivation* motifs that will ultimately increase blood pressure, but in parallel causes exploitation of the energy and nitrogen reservoirs in

skeletal muscle. Given the fact that even mild underlying glucocorticoid-driven catabolic states represent a major risk factor for adverse cardiovascular outcome and are strong predictors of increased mortality independent of their underlying cause,<sup>44</sup> we speculate that parallel catabolism might be an underestimated cause of adverse health events in patients and in experimental animals with arterial hypertension.

In summary, similar to our report in rats with chronic renal failure,<sup>4</sup> our findings in mice with chronic skin barrier failure define adaptive body responses to prevent dehydration as the underlying cause of elevated blood pressure and muscle mass loss. We anticipate that preclinical and clinical investigation of compensatory *aestivation* responses may shed new light on the pathogenesis of essential hypertension and muscle mass loss, which occur simultaneously in ageing populations. The skin is the largest organ of the human body; however, its importance as a physiological regulator of systemic energy and fluid metabolism may be underrated. Our findings indicate that the skin is a powerful contributor to systemic blood pressure homeostasis, and an easily assessable and potentially underestimated target for hypertension treatment.

## 4 | MATERIALS AND METHODS

### 4.1 | Animal studies

We conducted all animal experiments in accordance with institutional, state and federal guidelines and with permission of the local animal ethics committee (Responsible government institution: Landesuntersuchungsamt Rheinland-Pfalz; animal experiment permission numbers G17-1-076 and G15-1-101). Animal treatment was in accordance with the Guide for the Care and Use of Laboratory Animals as adopted by the US National Institutes of Health and was granted by the University Medical Center Mainz Ethics Committee. All mice were housed on a 12-hour light/dark cycle with constant access to food and tap water. We generated K14-IL-17A<sup>ind/+</sup> mice by crossing the IL-17A<sup>ind/ind</sup> allele (resulting from genetically changed Bruce-stemcells and backcrossed to C57Bl/6J over 50 generations) to the K14-Cre allele.<sup>14</sup> In K14-Cre mice, Cre-recombinase was shown to be expressed specifically in keratinocytes with only low background levels in the thymus.<sup>45</sup> For breeding, Cre gene was maintained only in the male mice. In the K14-IL-17A<sup>ind/+</sup> mouse strain, IL-17A (co-expressed with EGFP, enhanced green fluorescent protein) is overexpressed in the skin based on Cre-mediated recombination. K14-IL-17A<sup>ind/+</sup> mice invariably develop an overt skin inflammation bearing many hallmark characteristics of human psoriasis. As control group, we always used IL-17A<sup>ind/+</sup> litter mates with physiological IL-17A levels and

without skin deficits. We conducted the experiments with mice of 8-12 weeks of age.

### 4.2 | Transepidermal water loss

We depilated the mice 48 hours before measurements to avoid any influence of shaving-related skin irritation on the measurements. The fur was removed with an electric razor in an area on the chest and the back with a diameter of 1cm each, which equalled the diameter of the probe head of the Tewameter device. Anaesthesia was induced in a transparent chamber (2%-3.5% isoflurane mixed with 0.2-0.3 L/min 100% O<sub>2</sub>) and maintained by using a face mask (1%-2% isoflurane with 0.2 L/min 100% O<sub>2</sub>) under continuous monitoring of heart rate and body temperature on a heating plate, monitored by ECG electrodes and a rectal probe. Room temperature was continuously maintained at 21.0°C. We measured Transepidermal water loss (TEWL) with a Tewameter<sup>®</sup> TM300 (Courage & Khazaka, Cologne, Germany) on the back and the chest of the mice. The Tewameter<sup>®</sup> probe measures the density gradient of the water evaporation from the skin indirectly, so the open chamber method can measure TEWL continuously without influencing the skin microenvironment. A microprocessor analyses the values and expresses the evaporation rate in g/h/m<sup>2</sup>. We calculated body surface area (BSA) as  $9.822 \times \text{body weight}^{0.667}$ .<sup>46</sup> The following formula estimates daily transepidermal water loss: Transepidermal water loss per day in g = ((Area of affected skin [m<sup>2</sup>] × TEWL affected skin [g/h/m<sup>2</sup>]) + (Area of non-affected skin [m<sup>2</sup>] × TEWL non-affected skin [g/h/m<sup>2</sup>])) × 24 hours. We obtained the difference in total body water content of K14-IL-17A<sup>ind/+</sup> mice and healthy littermates by desiccation of tissue at 100 °C for 72 hours.

### 4.3 | Urine collection

We placed 8-9 week old animals into metabolic cages (Tecniplast Metabolics, Buguggiate, Italy) for 16-19 hours without access to food. We started the measurement for every animal at the same time of the day to avoid circadian differences. Bodyweight was measured before and after the period in the metabolic cage. During urine collection, mice had ad libitum access to water. We measured water intake, urine output and urine samples were collected for further analysis. We additionally monitored food and water consumption in the normal cages 24 hours before the metabolic cage experiments. In order to achieve the highest accuracy possible, we used brand new funnels for the experiments to exclude erosion of the hydrophobic coating of the funnels, which would lead to more adhesion of the urine to the funnel wall with

resulting increased evaporation. Additionally, we sealed the lid of the metabolic cage with adhesive tape.

#### 4.4 | Electrolyte and osmolality measurements

Sodium and potassium concentrations in plasma and urine were measured by flame photometry by the certified Central Laboratory of the University Medical Centre Mainz. Plasma and urine osmolality were calculated by determining the freezing point depression (Loeser, Berlin, Germany).

#### 4.5 | Laser Doppler perfusion imaging

For laser Doppler perfusion imaging of the skin, we used the PeriCam PSI NR System<sup>®</sup> (Perimed, Rommelskirchen, Germany). Mice underwent the same inhalation anaesthesia as afore mentioned and were placed on a heating plate in prone position. We taped the back paws firmly to the surface of the heating plate with the plantar side up, facilitating regulation of the paw temperature by the heating block. Temperature was monitored with an infrared thermometer (TW2 Pocket Infrared Thermometer ThermoWorks, Salt Lake City, USA). After adjustment of the appropriate distance for the laser, we imaged the plantar side of both paws serially twice with the identical image size of 4.5-4.7 × 2.4-2.6 cm. For the first measurement, the heating plate was kept at room temperature (21°C), for the second measurement, the temperature was set to 40°C. The mean perfusion of both images averaged for both paws is presented.

#### 4.6 | Heating experiment

Mice were depilated 48h hours before measurements. We induced inhalation anaesthesia as afore mentioned and placed the mice on a heated table mounted on a rail system (Fujifilm VisualSonics, Toronto, Ontario), monitored by ECG electrodes and a rectal probe. Room temperature was maintained at 21.0°C. After establishing a stable anaesthesia monitored by heart rate and a constant core temperature of 36°C, we exposed the mice to red light at a distance of 30-50 cm to heat the animals from 36°C to 40°C body core temperature within 15 minutes. Body core temperature was continuously monitored with a rectal probe. During the heating period, TEWL was measured with a Tewameter<sup>®</sup> TM300 (Courage & Khazaka, Cologne, Germany) as described above. Furthermore, blood pressure

and renal resistive index were measured in parallel as described below. In preliminary studies, continuous measurements with the Tewameter device on the skin of the animals blocked the transmission of the red light to their body surface. This negatively affected the heating process. Therefore, we measured blood pressure, renal resistive index and TEWL directly before the heating process, only once during the heating period (at minute 5) and after 15 minutes which was the endpoint of the experiment to achieve a reliable temperature increase.

#### 4.7 | Determination of blood pressure

Systolic blood pressure was obtained in mice using a tail cuff noninvasive blood pressure system with the CODA<sup>®</sup> High Throughput System (Kent Scientific, Torrington, USA) as previously published.<sup>47</sup> The mice were placed on the heated table without a restrainer. During the heating period, we continuously performed repeated measurements over 30 seconds without any pauses between the measurements. We decided to use this way of estimating a blood pressure time course, because the extent of skin disease in K14-IL-17A<sup>ind/+</sup> mice did not allow us to use invasive blood measurement by telemetric catheter implantation, as severe manipulations of the diseased skin are lethal for the animals and therefore not appropriate according to the 3R-guidelines of laboratory animal handling. We accepted the limitation that systolic arterial pressure is more sensitive to changes in stroke volume than to vascular resistance. We were keen on limiting the heating experiment to the shortest period possible, so that the effect of the anaesthesia on vascular tone would not induce a blood pressure drop and mild hypothermia. We therefore selected non-invasive tail cuff measurements for comparative blood pressure recordings between the groups.

#### 4.8 | Renal resistive index

For high-resolution ultrasound imaging, we used the Vevo3100 Imaging System (Fujifilm VisualSonics, Toronto, Canada). Renal perfusion was measured as published before.<sup>48,49</sup> We placed the transducer on the abdominal area of the mice and acquired longitudinal images of the right kidney. We visualized one lower and one upper interlobar artery with Color Doppler. Blood flow velocity in Pulse Wave Doppler Mode and parallel color Doppler images were acquired. The mean of three measurements in two different interlobar arteries each were assessed. The renal resistive index was calculated with the following formula: Renal resistive index = (Peak systolic velocity – end diastolic velocity)/ peak systolic velocity.



#### 4.9 | Intravital microscopy of intra-renal urine flow

For anaesthesia, we used midazolam ( $5 \text{ mg kg}^{-1}$ ), medetomidine ( $0.5 \text{ mg kg}^{-1}$ ) and fentanyl ( $0.05 \text{ mg kg}^{-1}$ ) and fixed the mice on a custom-built stage. The microscope stage and the animals were warmed using a heating pad during all experimental procedures. We implanted a jugular vein catheter (inner diameter 0.28 mm; outer diameter 0.61 mm; Smiths Medical Deutschland GmbH, Grasbrunn, Germany), exteriorized the left kidney through a small flank incision and affixed the kidney to a coverslip. Tubular flow was visualized by an upright confocal spinning disc microscope (Nikon Instruments Europe, Amsterdam, Netherlands) including a spinning disc unit (CSU-W1, Yokogawa, Tokyo, Japan), sCMOS 4.2 megapixels cameras (Zyla 4.2 plus, Oxford Instruments Andor, Abingdon, UK), 25x water immersion objective (CFI-75 Apo 25x, numerical aperture 1.10, Nikon) and laser beamcombiner (ILE-Beamcombiner, Nikon). The imaging setting for the microscope (gain and offset for all three channels; blue, green, and red) was fixed throughout the experiment. For visualizing tubular flow, we followed the protocol of Kitamura et al<sup>50</sup>: Lucifer yellow ( $100 \mu\text{g kg}^{-1}$ , intravenous bolus, L0259, Merck, Kenilworth, USA), a dye freely filtered by glomeruli, was injected via the jugular catheter. Time-lapse images for tubular flow measurements were taken starting directly after the injection via the jugular catheter. The inflow time of Lucifer yellow was defined as the time to peak fluorescence intensity and measured in proximal and distal segments of three spatially separated tubular lumens that showed Lucifer yellow the earliest in each imaging window. We measured the distance between the proximal and the distal point as well as the radius of the proximal tubule. We calculated tubular flow rate:  $\text{flow rate} = \text{distance} \times \text{radius}^2 \times \pi / (\text{inflow time distal part of proximal tubule} - \text{inflow time proximal part of proximal tubule})$ . Since these tubules are early segments of proximal tubules, the tubular flow time reflects glomerular filtration rate. We measured the passage time from proximal to distal tubules by taking the inflow time of Lucifer yellow in proximal segment of three spatially separated proximal tubular lumens and the inflow time in three distal nephrons per animal.

#### 4.10 | Tissue water content

We dissected the mice into skin and skinned carcasses and measured tissue water by desiccation of tissue at  $100^\circ\text{C}$  for 72 hours as reported previously.<sup>51,52</sup> Water content was calculated from the difference between wet weight and dry weight.

#### 4.11 | Histology

For haematoxylin and eosin staining, tissues were dissected and fixed in 4% paraformaldehyde, paraffin-embedded, cut and stained with haematoxylin and eosin according to standard protocols. Cryo-sections of the skin (5–8  $\mu\text{m}$  thickness) were fixed with 4%PFA and permeabilized by 0.1%–0.2% Triton X-100 for 10 minutes. After blocking with 5%BSA, tissue was co-stained with rabbit polyclonal antibody against TonEBP (PA1-023, Invitrogen Life Technologies, Carlsbad, USA) and anti-CD45 (ab10558, Abcam, Cambridge, UK) or anti-Glucocorticoid Receptor (D6H2L, 12041, Cell Signaling, Cambridge, UK). After overnight incubation, sections were counterstained with the secondary antibodies (donkey anti-rabbit IgG (ab150076, Abcam), and goat anti-mouse IgG, (ab150116, Abcam) and mounted in anti-fading mounting medium for confocal laser scanning. Nuclei were counterstained with Hoechst 3342 (Invitrogen). Microscopy was performed by confocal laser scanning or by using the fluorescence microscope Olympus IX81 and the TSA Cy3 and TSA Fluorescein system (Perkin Elmer, Waltham, USA) as recommended by the company.

#### 4.12 | Kidney histological evaluation

One kidney per mouse was fixed and stained with haematoxylin and eosin. The stainings were performed by the Histology Core Facility of the Institute of Molecular Biology (University of Mainz, Germany). To determine kidney injury, 10 consecutive cortical and juxtamedullary images per animal were taken using an Olympus IX73 microscope and an Olympus SC30 camera (Olympus, Tokyo, Japan) and were examined. Quantitative analysis of kidney injury was determined by semiquantitative injury scoring (ATN score: 0,  $\leq 5\%$ ; 1, 5%–15%; 2, 15%–25%; 3, 25%–50%; 4,  $\geq 50\%$ ). These examinations were performed blinded.

#### 4.13 | Angiotensin II, metanephrine, creatinine and protein measurements

We measured serum angiotensin II and metanephrine levels by enzyme-linked immunosorbent assay with commercially available kits according to the manufacturer's protocols. (Angiotensin II: EKV02406, Biomatik, Wilmington, USA; Metanephrine: MBS265523, MyBioSource, San Diego, USA). Creatinine in urine samples was measured by a coupled enzyme reaction following manufacturer's recommendations (MAK080, Creatinine Assay Kit, Sigma-Aldrich). We measured urine protein content by Bradford assay using Roti-Quant (K015.1, Carl Roth, Karlsruhe, Germany).

Proteinuria was calculated as milligram of protein per milligram of creatinine.

#### 4.14 | Urea and enzyme activity assays

Tissue was homogenized in protein extraction reagent (78510, Thermo Fisher, Waltham, USA) supplemented with protease/phosphatase inhibitor cocktail (1861280, Thermo Fisher) using an Omni TH homogenizer (Omni, Kennesaw, USA) immediately after tissue collection. After homogenization, we centrifuged the samples at 15 000× *g* for 20 minutes. To extract urea from protein, the samples were filtered with a 10-kDa molecular weight cut-off spin column (UFC505096, EMD Millipore, Merck). We took the urea-depleted supernatant for measuring arginase activity, malate dehydrogenase 1 activity and aspartate aminotransferase activity with commercially available kits according to the manufacturer's protocols (Arginase: MAK112, Sigma-Aldrich; Malate dehydrogenase 1: ab200009, Abcam; Aspartate aminotransferase: ab105135, Abcam). We measured urea concentration in urine, plasma and tissues by colorimetry with a urea assay kit (K375, BioVision, Milpitas, USA).

#### 4.15 | Metabolomic profile analysis

##### 4.15.1 | Sample preparation

Liver and muscle samples from K14-IL-17A<sup>ind/+</sup> mice and IL-17A<sup>ind/+</sup> litter mates at the age of 8 weeks, were washed with PBS, snap-frozen in liquid nitrogen and stored at −80°C till metabolites extraction. The samples of approximately 100 mg were manually grounded in liquid nitrogen using a mortar kept in dry ice. Ice-cold CHCl<sub>3</sub>/MeOH (2:1) solution was added to (1 mL for 100 mg) to the frozen tissue powder and sonicated in an ice/water US bath for 5 minutes. Then, an equivalent volume (1 mL) of cold HPLC-grade water was added, the homogenate was vortex mixed for 1 minutes, kept on ice for 15 minutes, and centrifuged for 10 minutes at 4°C at 2000 *g*, separating the two phases (chloroform and water/methanol). The two fractions were collected and stored at −20°C; the extraction procedure was repeated to maximize the metabolite yield, and the isolated fractions were pooled. The solvents were removed using a speed vacuum concentrator, and the dry extracts were stored at −80°C until analysis. The polar metabolites were reconstituted in 700 μL 99.9% D<sub>2</sub>O at pH 7.4 phosphate buffered saline (150 mmol/L) containing 0.01% 1,1,2,2-tetradeutero-3-trimethylsilylpropionic acid (TSP) as internal standard and 0.2 mmol/L Na<sub>3</sub>N for microbial growth inhibition.

##### 4.15.2 | NMR spectroscopy

Metabolic profiling has been performed using NMR spectroscopy. All NMR spectra were acquired on a 600 MHz Avance III spectrometer (Bruker, Billerica, USA) equipped with a B-ACS60 sample changer at temperature probe 27°C. Sample loading, temperature stabilization, field homogeneity, pulse calibration, data acquisition and processing, including Fourier transformation, phase and baseline correction, and axis calibration were accomplished from the ICONNMR program suite (TopSpin v. 3.5, Bruker Biospin GmbH). For each sample, 1D NOESY (noesygp1d, Bruker library) and J-resolved (JRES) spectra were acquired with water signal suppression during relaxation and mixing time. 1D NOESY spectra were recorded with 192 free induction decays (FIDs) with 64k data points at a spectral width of 12335 Hz, with acquisition time of 2.7 seconds, relaxation delay 6 seconds and mixing time 0.010 seconds. The J-resolved spectra were acquired with 8k points, 40 increments of 8 scans each, for a spectral width of 10 000 Hz and a J-coupling domain spectral width of 78 Hz. The NMR spectra handling was performed with TOPSPIN v. 3.1 software (Bruker BioSpin). Metabolite signals assignment was performed with the aid of the Chemomx software (NMR suit 8.3, Chenomx Inc) and the freely available electronic Human Metabolome Database (HMDB, <https://hmdb.ca>). A detailed list of the assigned metabolites (51 in total) is provided in Online Table S3. Representative <sup>1</sup>H NMR spectra of polar metabolites extracted from the liver and muscle tissue of a K14-IL-17A<sup>ind/+</sup> mouse are presented in Online Figure S9. NMR spectra (spectral width from 9.50 to 0.60 ppm) were segmented into 1737 chemical shift regions of 0.005 ppm width, using the software package AMIX Statistics v. 3.9.14 (Analysis of MIXtures, Bruker BioSpin), the integrals were calculated and normalized to the total intensity. The region of the residual water suppression trace (4.90–4.68 ppm) was excluded from the data set.

#### 4.16 | Quantitative real-time reverse-transcription polymerase chain reaction (real-time RT-PCR)

Total RNA extraction was performed using the standardized method of Trizol isolation as previously shown.<sup>42</sup> Briefly, we lysed and homogenized the tissues in TRIzol<sup>®</sup> (15 596 026, Thermo Fisher) along manufacturer's protocol. RNA concentration was measured using the NanoDrop spectrophotometer (Thermo Fisher). 0.5 μg of total RNA was used for quantitative real-time PCR (qPCR). For QuantiTect SYBR Green RT-PCRs, one microgram of cDNA was measured. The QuantiTect SYBR Green

reaction mixture (204245, Qiagen, Venlo, Netherlands) was used on RT-PCR 96-well plates (Roche) with primer mixes from Qiagen as described on their homepage. For the quantification of mRNA expression, we used the comparative delta CT method. The gene expression was normalized to the endogenous control (GAPDH mRNA) and the expression of target gene mRNA of each sample was expressed relative to that of control.

The following primers were used for QuantiTec-SYBR Green TR-PCRs:

Aquaporin 1<sup>53</sup>  
 forward 5'-GCTTGCCATTGGCTTGTCTG-3'/reverse  
 5'-TGGTTTGAGAAGTTGCGGGT-3'

Aquaporin 2<sup>54</sup>  
 forward 5'-GTGGGTTGCCATGTCTCCTT-3'/reverse  
 5'-GTCCCCGCGGATTTCTACAG-3'

Aquaporin 3  
 forward 5'-GCCCTCCAGAATTTCTATGAACTCT-3'/  
 reverse 5'-TTTGCTATCCTACCTTGGCTTAAAG-3'

Aquaporin 4  
 forward 5'-GGGAGAGGTATTGTCTTCCGTATG-3'/re-  
 verse 5'-ATGGGTGGCAGGAAATCTGA-3'

UT-A1  
 forward 5'-GACAGTGAGACGCAGTGAAG-3'/reverse  
 5'-ACGGTCTCAGAGCTCTCTTC-3'

UT-A2  
 forward 5'-TTTCTCCAGTCCTATCTGAG-3'/reverse  
 5'-ACGGTCTCAGAGCTCTCTTC-3'

UT-A3  
 forward 5'-ACGGTCTCAGAGCTCTCTTC-3'/reverse  
 5'-AGAGTGGAGGCCACACGGAT-3'

#### 4.17 | Western blot analysis

For western blot analyses, tissues were mechanically homogenized after snap freezing in liquid nitrogen. The tissue homogenates were adjusted for protein content using Bradford assay, separated by SDS-PAGE, then electroblotted onto PVDF membranes (EMD Millipore). Membranes were subsequently incubated overnight at 4°C with the following commercially available primary antibodies: rabbit polyclonal anti-p-AMPK $\alpha$  (Thr172) antibody (1:1000; Cell Signaling Technology; 4188); rabbit polyclonal anti-AMPK $\alpha$  antibody (1:1000; Cell Signaling Technology; 1532), anti- $\alpha$ -actinin (1:10 000; Cell Signaling; 3134), anti- $\beta$ -actin (1:10 000; Sigma-Aldrich; A3854) or anti-GAPDH antibody (1:10 000; Sigma-Aldrich; G9295), anti-UT-A1 antibody (StressMarq Biosciences; SPC-406D), rabbit polyclonal anti-TonEBP antibody (1:1000; Invitrogen; PA1-023). Detection was performed by ECL with peroxidase conjugated anti-rabbit/mouse secondary antibodies (1:5000; Cell Signaling Technology;

7074/7076). Immunodetection was fulfilled with ECL Reagent (34577, Thermo Fisher) and a Fusion FX reader (Vilber, Munich, Germany). Antibody-specific bands were finally quantified by densitometry with FUSION FX software (Vilber).

#### 4.18 | Chemicals

All chemicals were of highest analytical grade from Sigma-Aldrich/Merck unless otherwise stated.

#### 4.19 | Human study

All the studied individuals were psoriasis patients of the outpatient clinic of the Department of Dermatology at the University Medical Center Mainz who were enrolled for a regular appointment. All participants gave informed written consent to laboratory analyses, clinical examinations, sampling of biomaterial and the use of data records for research purposes. Exclusion criteria were insufficient knowledge of German language and physical or psychological inability to participate in the examinations. The study was designed according to the tenets of the revised Helsinki protocol and protocol and sampling design were approved by the local ethics committee and by the local and federal data safety commissioners (Ethics committee Rhineland-Palatinate, Germany, approval number 2018-13105-KliFo). After informed consent, a specialist for dermatology performed clinical examination including PASI scoring. Afterwards, transepidermal water loss (TEWL) was measured with the same Tewameter® TM300 (Courage & Khazaka, Cologne, Germany) as used in the murine studies. All measurements were taken in the same climatized examination room at a room temperature of 21°C. For each site, we obtained three consecutive measurements and calculated the mean.

#### 4.20 | Statistical analysis

Power calculation as basis for any animal experiment according to the federal animal law and was performed using G\*Power Software Version 3.1.9.2 (HHU Duesseldorf, Duesseldorf, Germany). Effect sizes were calculated from previously published experiments. All findings shown have been reproduced in at least two independent experiments. Concerning the metabolites derived from the NMR data, buckets integrals generated by AMIX software, normalized to spectral total intensity (NMR spectroscopy paragraph) were used to calculate signal intensities. Depending on the region overlap, one bucket or the sum of buckets were used for metabolites statistical analysis. Data are presented

depending on their scale and distribution with arithmetic mean and standard deviation (mean  $\pm$  SEM) or median including 25%-75% quartiles (25|75). Unless otherwise specified, boxplots show median and interquartile range (IQR) with whiskers showing minimum and maximum values, bar graphs show individual values and mean  $\pm$  SEM. Outliers identified by ROUT or Grubbs' test were excluded. Normality was assessed by Kolmogorov-Smirnov normality test. To compare independent measurements, we used two-tailed unpaired student's *t*-test and Mann-Whitney *U* test, as appropriate. To compare dependent measurements, we used a paired *t* test or Wilcoxon signed-rank test, as appropriate. To compare more than two groups, we used one-way ANOVA followed by Tukey's post-hoc test or Kruskal-Wallis test followed by Dunn's post hoc test, as appropriate. Statistical analysis was performed using GraphPad Prism 8 (version 8; GraphPad Software, Inc, La Jolla, USA). *P*-values of  $P \leq .05$  were considered statistically significant.

## ACKNOWLEDGEMENTS

This study was funded by the Boehringer Ingelheim Foundation "Novel and neglected cardiovascular risk factors: molecular mechanisms and therapeutic implications" (SK, JW, PW and TM). JW is supported by the German Federal Ministry for Education and Research (BMBF EDU-V24) and the University of Mainz ('Inneruniversitäre Forschungsförderung'). SK was supported by the German Research Foundation (DFG KA 4035/1-1). SK and PW received funding by the Federal Ministry of Education and Research (BMBF 01EO1503) related to this study. SK and AW were supported by the CRC/Transregio 156 ("The Skin as Sensor and Effector Organ Orchestrating Local and Systemic Immune Responses", DFG). JT was supported by grants from the German Federal Ministry for Economics and Technology/DLR Forschung unter Weltraumbedingungen (Mars500-III; 50WB2024), the NIH (RO1 HL118579), the Renal Research Institute, and an institutional start-up block fund from Duke-NUS. KK was supported by an Overseas Fellowship from the Japan Society for the Promotion of Science. We are grateful to Katharina Perius, Anne-Kristin Conze, Alexej Nikolaev, Annika Jurda and Ruth Teuber for excellent technical assistance. We thank Andrew Croford for the IL-17A<sup>ind/+</sup> mouse strain, Magdalena Bochenek for instructions to visualize skin blood flow and Daniel Sollinger for help and advice. We are indebted to our study participants.

## CONFLICT OF INTERESTS

The authors declare no competing interests.

## AUTHOR CONTRIBUTIONS

JW designed and performed experiments, analyzed data, performed statistical analysis, designed figures and wrote the

first draft of the manuscript. RJ, TK, PE, DB, AG, MM, VG, NR and LM contributed to data acquisition and analysis. JW acquired parts of human data set. AM and KK were involved in development of the research hypothesis and experimental design. EM and MR contributed specific data acquisition and analysis of metabolomics. DN helped with the experimental design of intravital imaging experiments. TM supplied scientific infrastructure. SK contributed to data analysis and figure design. FL edited and revised the manuscript. AW provided scientific infrastructure, funding and K14-IL-17A<sup>ind/+</sup> mice. PW provided scientific infrastructure and funding. SK supervised specific data acquisition and analysis, revised the manuscript and provided funding. JT articulated the research hypothesis, designed the research approach and wrote the manuscript. All authors read and approved the final version of the manuscript.

## DATA AVAILABILITY STATEMENT

All data generated or analysed during this study are included in the manuscript (and its supplementary information files).

## ORCID

Johannes Wild  <https://orcid.org/0000-0002-1446-8101>  
 Rebecca Jung  <https://orcid.org/0000-0002-2460-6512>  
 Michael Molitor  <https://orcid.org/0000-0001-6075-4996>  
 Adriana Marton  <https://orcid.org/0000-0002-7702-1577>  
 Thomas Münzel  <https://orcid.org/0000-0001-5503-4150>  
 Sabine Kossmann  <https://orcid.org/0000-0002-1403-0978>  
 Friedrich Luft  <https://orcid.org/0000-0002-8635-1199>  
 Philip Wenzel  <https://orcid.org/0000-0002-5397-2781>  
 Jens Titze  <https://orcid.org/0000-0001-8463-8404>  
 Susanne Karbach  <https://orcid.org/0000-0003-4462-3747>

## REFERENCES

1. Borst JG, Borst-De GA. Hypertension explained by Starling's theory of circulatory homeostasis. *Lancet*. 1963;1(7283):677-682.
2. Coleman TG, Guyton AC. Hypertension caused by salt loading in the dog. 3. Onset transients of cardiac output and other circulatory variables. *Circ Res*. 1969;25(2):153-160.
3. Freis ED. Salt, volume and the prevention of hypertension. *Circulation*. 1976;53(4):589-595.
4. Kovarik J, Morisawa N, Wild J, et al. Adaptive physiological water conservation explains hypertension and muscle catabolism in experimental chronic renal failure. *Acta Physiol (Oxf)*. 2021:e13629. <https://doi.org/10.1111/apha.13629>
5. Burggren WW, Vitalis TZ. The interplay of cutaneous water loss, gas exchange and blood flow in the toad, *Bufo woodhousei*: adaptations in a terrestrially adapted amphibian. *J Exp Biol*. 2005;208 (Pt 1):105-112.
6. Hembree DI. Aestivation in the fossil record: evidence from ichnology. *Prog Mol Subcell Biol*. 2010;49:245-262.
7. Storey KB, Storey JM. Metabolic regulation and gene expression during aestivation. *Prog Mol Subcell Biol*. 2010;49:25-45.



8. Storey KB, Storey JM. Aestivation: signaling and hypometabolism. *J Exp Biol.* 2012;215(Pt 9):1425-1433.
9. Delaney RG, Lahiri S, Fishman AP. Aestivation of the African lungfish *Protopterus aethiopicus*: cardiovascular and respiratory functions. *J Exp Biol.* 1974;61(1):111-128.
10. Szidon JP, Lahiri S, Lev M, Fishman AP. Heart and circulation of the African lungfish. *Circ Res.* 1969;25(1):23-38.
11. Hanel KH, Cornelissen C, Luscher B, Baron JM. Cytokines and the skin barrier. *Int J Mol Sci.* 2013;14(4):6720-6745.
12. Mosteller RD. Simplified calculation of body-surface area. *N Engl J Med.* 1987;317(17):1098.
13. Ramos-e-Silva M, Jacques C. Epidermal barrier function and systemic diseases. *Clin Dermatol.* 2012;30(3):277-279.
14. Croxford AL, Karbach S, Kurschus FC, et al. IL-6 regulates neutrophil microabscess formation in IL-17A-driven psoriasisiform lesions. *J Invest Dermatol.* 2014;134(3):728-735.
15. Goh CL, Khoo L. Laser Doppler perfusion imaging (LDPI) and transepidermal water loss (TEWL) values in psoriatic lesions treated with narrow band UVB phototherapy. Dermal vascularity may be useful indicator of psoriatic activity. *Ann Acad Med Singapore.* 2004;33(1):75-79.
16. Navas CA, Carvalho JE. *Aestivation: Molecular and physiological aspects.* Heidelberg: Springer Verlag; 2010.
17. Kriz W. Structural organization of the renal medulla: comparative and functional aspects. *Am J Physiol.* 1981;241(1):R3-R16.
18. Sands JM. Critical role of urea in the urine-concentrating mechanism. *J Am Soc Nephrol.* 2007;18(3):670-671.
19. Nakayama Y, Peng T, Sands JM, Bagnasco SM. The TonE/TonEBP pathway mediates tonicity-responsive regulation of UT-A urea transporter expression. *J Biol Chem.* 2000;275(49):38275-38280.
20. Hasler U, Jeon US, Kim JA, et al. Tonicity-responsive enhancer binding protein is an essential regulator of aquaporin-2 expression in renal collecting duct principal cells. *J Am Soc Nephrol.* 2006;17(6):1521-1531.
21. Ho SN. Intracellular water homeostasis and the mammalian cellular osmotic stress response. *J Cell Physiol.* 2006;206(1):9-15.
22. Kim YM, Kim WY, Lee HW, et al. Urea and NaCl regulate UT-A1 urea transporter in opposing directions via TonEBP pathway during osmotic diuresis. *Am J Physiol Renal Physiol.* 2009;296(1):F67-F77.
23. Jung JY, Kwon HM, Kim J. Regulation of urea transporters by tonicity-responsive enhancer binding protein. *Electrolyte Blood Press.* 2007;5(1):28-33.
24. Sebastian R, Chau E, Fillmore P, et al. Epidermal aquaporin-3 is increased in the cutaneous burn wound. *Burns.* 2015;41(4):843-847.
25. Machnik A, Neuhofer W, Jantsch J, et al. Macrophages regulate salt-dependent volume and blood pressure by a vascular endothelial growth factor-C-dependent buffering mechanism. *Nat Med.* 2009;15(5):545-552.
26. Wiig H, Schroder A, Neuhofer W, et al. Immune cells control skin lymphatic electrolyte homeostasis and blood pressure. *J Clin Invest.* 2013;123(7):2803-2815.
27. Karbach S, Croxford AL, Oelze M, et al. Interleukin 17 drives vascular inflammation, endothelial dysfunction, and arterial hypertension in psoriasis-like skin disease. *Arterioscler Thromb Vasc Biol.* 2014;34(12):2658-2668.
28. Forslind B. The skin barrier: analysis of physiologically important elements and trace elements. *Acta Derm Venereol Suppl (Stockh).* 2000;208:46-52.
29. Wei X, Roomans GM, Forslind B. Elemental distribution in guinea-pig skin as revealed by X-ray microanalysis in the scanning transmission microscope. *J Invest Dermatol.* 1982;79(3):167-169.
30. Forslind B, Roomans GM, Carlsson LE, Malmqvist KG, Akselsson KR. Elemental analysis on freeze-dried sections of human skin: studies by electron microprobe and particle induced X-ray emission analysis. *Scan Electron Microsc.* 1984;Pt 2(2):755-759.
31. von Zglinicki T, Lindberg M, Roomans GM, Forslind B. Water and ion distribution profiles in human skin. *Acta Derm Venereol.* 1993;73(5):340-343.
32. Forslind B, Lindberg M, Malmqvist KG, Pallon J, Roomans GM, Werner-Linde Y. Human skin physiology studied by particle probe microanalysis. *Scanning Microsc.* 1995;9(4):1011-1025.discussion 1025-1016.
33. Forslind B, Engstrom S, Engblom J, Norlen L. A novel approach to the understanding of human skin barrier function. *J Dermatol Sci.* 1997;14(2):115-125.
34. Forslind B, Lindberg M, Roomans GM, Pallon J, Werner-Linde Y. Aspects on the physiology of human skin: studies using particle probe analysis. *Microsc Res Tech.* 1997;38(4):373-386.
35. Kitada K, Daub S, Zhang Y, et al. High salt intake reprioritizes osmolyte and energy metabolism for body fluid conservation. *J Clin Invest.* 2017;127(5):1944-1959.
36. Felig P. The glucose-alanine cycle. *Metabolism.* 1973;22(2):179-207.
37. Felig P, Owen OE, Wahren J, Cahill GF Jr. Amino acid metabolism during prolonged starvation. *J Clin Invest.* 1969;48(3):584-594.
38. Arendshorst WJ, Gottschalk CW. Glomerular ultrafiltration dynamics: historical perspective. *Am J Physiol.* 1985;248(2 Pt 2):F163-174.
39. Buraczewska I, Berne B, Lindberg M, Torma H, Loden M. Changes in skin barrier function following long-term treatment with moisturizers, a randomized controlled trial. *Br J Dermatol.* 2007;156(3):492-498.
40. Smith CJ, Johnson JM. Responses to hyperthermia. Optimizing heat dissipation by convection and evaporation: Neural control of skin blood flow and sweating in humans. *Auton Neurosci.* 2016;196:25-36.
41. Yosipovitch G, Sackett-Lundeen L, Goon A, Yiong Huak C, Leok Goh C, Haus E. Circadian and ultradian (12 h) variations of skin blood flow and barrier function in non-irritated and irritated skin-effect of topical corticosteroids. *J Invest Dermatol.* 2004;122(3):824-829.
42. Schuler R, Efentakis P, Wild J, et al. T cell-derived IL-17A induces vascular dysfunction via perivascular fibrosis formation and dysregulation of (.)NO/cGMP signaling. *Oxid Med Cell Longev.* 2019;2019:6721531.
43. Johnson JM, Minson CT, Kellogg DL Jr. Cutaneous vasodilator and vasoconstrictor mechanisms in temperature regulation. *Compr Physiol.* 2014;4(1):33-89.
44. Goddard GM, Ravikumar A, Levine AC. Adrenal mild hypercortisolism. *Endocrinol Metab Clin North Am.* 2015;44(2):371-379.
45. Hafner M, Wenk J, Nenci A, et al. Keratin 14 Cre transgenic mice authenticate keratin 14 as an oocyte-expressed protein. *Genesis.* 2004;38(4):176-181.
46. Cheung MC, Spalding PB, Gutierrez JC, et al. Body surface area prediction in normal, hypermuscular, and obese mice. *J Surg Res.* 2009;153(2):326-331.
47. Kossmann S, Lagrange J, Jackel S, et al. Platelet-localized FXI promotes a vascular coagulation-inflammatory circuit in arterial hypertension. *Sci Transl Med.* 2017;9(375):eaah4923.

48. Viazzi F, Leoncini G, Derchi LE, Pontremoli R. Ultrasound Doppler renal resistive index: a useful tool for the management of the hypertensive patient. *J Hypertens*. 2014;32(1):149-153.
49. Xu H, Ma Z, Lu S, et al. Renal Resistive Index as a Novel Indicator for Renal Complications in High-Fat Diet-Fed Mice. *Kidney Blood Press Res*. 2017;42(6):1128-1140.
50. Kitamura H, Nakano D, Sawanobori Y, et al. Guanylyl cyclase A in both renal proximal tubular and vascular endothelial cells protects the kidney against acute injury in rodent experimental endotoxemia models. *Anesthesiology*. 2018;129(2):296-310.
51. Titze J, Bauer K, Schafflhuber M, et al. Internal sodium balance in DOCA-salt rats: a body composition study. *Am J Physiol Renal Physiol*. 2005;289(4):F793-802.
52. Titze J, Lang R, Ilies C, et al. Osmotically inactive skin Na<sup>+</sup> storage in rats. *Am J Physiol Renal Physiol*. 2003;285(6):F1108-F1117.
53. Bouley R, Palomino Z, Tang SS, et al. Angiotensin II and hypertonicity modulate proximal tubular aquaporin 1 expression. *Am J Physiol Renal Physiol*. 2009;297(6):F1575-F1586.
54. Li C, Wang W, Rivard CJ, Lanaspá MA, Summer S, Schrier RW. Molecular mechanisms of angiotensin II stimulation on aquaporin-2 expression and trafficking. *Am J Physiol Renal Physiol*. 2011;300(5):F1255-F1261.

## SUPPORTING INFORMATION

Additional Supporting Information may be found online in the Supporting Information section.

**How to cite this article:** Wild J, Jung R, Knopp T, et al. *Aestivation* motifs explain hypertension and muscle mass loss in mice with psoriatic skin barrier defect. *Acta Physiol*. 2021;232:e13628. <https://doi.org/10.1111/apha.13628>